ADVANCED FUNCTIONAL MATERIALS
www.afm-journal.de

www.MaterialsViews.com

3D Interconnected Porous Carbon Aerogels as Sulfur Immobilizers for Sulfur Impregnation for Lithium-Sulfur Batteries with High Rate Capability and Cycling Stability

Zhiwei Zhang, Zhaoqiang Li, Fengbin Hao, Xuekun Wang, Qun Li, Yongxin Qi, Runhua Fan, and Longwei Yin**

To eliminate capacity-fading effects due to the loss of sulfur cathode materials as a result of polysulfide dissolution in lithium–sulfur (Li–S) cells, 3D carbon aerogel (CA) materials with abundant narrow micropores can be utilized as an immobilizer host for sulfur impregnation. The effects of S incorporation on microstructure, surface area, pore size distribution, and pore volume of the S/CA hybrids are studied. The electrochemical performance of the S/CA hybrids is investigated using electrochemical impedance spectroscopy, galvanostatical charge–discharge, and cyclic voltammetry techniques. The 3D porous S/CA hybrids exhibit significantly improved reversible capacity, high-rate capability, and excellent cycling performance as a cathode electrode for Li–S batteries. The S/CA hybrid with an optimal incorporating content of 27% S shows an excellent reversible capacity of 820 mAhg^{-1} after 50 cycles at a current density of 100 mAg^{-1}. Even at a current density of 3.2C (5280 mAg^{-1}), the reversible capacity of 27%S/CA hybrid can still maintain at 521 mAhg^{-1} after 50 cycles. This strategy for the S/CA hybrids as cathode materials to utilize the abundant micropores for sulfur immobilizers for sulfur impregnation for Li–S battery offers a new way to solve the long-term reversibility obstacle and provides guidelines for designing cathode electrode architectures.

1. Introduction

The improvement of rechargeable battery technologies to high-capacity energy storage systems for satisfying the emerging plug-in hybrid vehicle and electric vehicles are attracting much attention from the viewpoint of both energy and environmental issues. Li-ion batteries display variety of applications in transformed portable electronic devices and electric transportation greatly,[1,2] but have limitation of high cost and relatively low specific capacity and low energy density.[3,4] One of the most promising candidates for storage devices is the lithium-sulfur (Li-S) batteries. Sulfur can theoretically accept 2e$^-$ per atom leading to a capacity of 1675 mAhg^{-1}, which is an order of magnitude higher than that of conventional cathode materials (i.e., $LiCoO_2$, $LiMn_2O_4$, and $LiFePO_4$). The Li-S cell in its simplest configuration consists of sulfur as the positive electrode and lithium as the negative electrode.[5] The multi-electron-transfer cathode reaction, $S_8 + 16Li^+ + 16e^- = 8Li_2S$, offers an extremely high capacity of 1675 mAhg^{-1}, about five times the theoretical upper limit (300 mAhg^{-1}) for metal oxide cathode materials.[6] Moreover, Li-S battery is made with abundant and nonpoisonous sulfur that is a common byproduct of the petroleum refining process.

Despite the great promises, there still exist a number of complex obstacles that need to be tackled for the commercialization of Li-S batteries. The commercialization of Li-S batteries is mainly hampered by the following three major problems.[7] (i) The dissolution of the polysulfides in the electrolyte forming deposits of solid Li_2S_2 and Li_2S on the cathode, causes the redox shuttle between the anode and the cathode and severe loss of usable active material.[8,9] (ii) Moreover, the soluble polysulfide deposits as Li_2S_2/Li_2S on the cathode surface, may hinder the lithium ion migration and reducing the electrode conductivity, leading to low Coulombic efficiency, low utilization of the sulfur cathode, and a severe degradation of cycle life. (iii) The low electrical conductivity of sulfur, the intermediate polysulfide products, and the final Li_2S, may greatly reduce the reaction rate of the battery. As is known, elemental sulfur is inherently insulating to both electrons and lithium ions. The electronic conductivity of sulfur at room temperature is 5×10^{-30} S cm^{-1}, more than 20 orders of magnitude lower than that of normal lithium transition-metal oxides.[7] These three challenging problems result in severely degraded capacity at large current drain and poor cycling stability.

In order to overcome the obstacles, several technological contributions were attempted. The first one was to physically restrain polysulfide dissolution using barrier materials. The physical restraint methods include carbon coating on sulfur,[10] high surface-area carbon additives,[11] and polymeric electrolytes.[12] The most promising physical restraint methods

Z. Zhang, Z. Li, F. Hao, X. Wang, Q. Li,
Prof. Y. X. Qi, R. Fan, Prof. L. W. Yin
Key Laboratory for Liquid–Solid Structural Evolution and Processing of Materials
Ministry of Education
School of Materials Science and Engineering
Shandong University
Jinan, 250061, PR China
Tel.: + 86 531 88396970; Fax: + 86 531 88396970
E-mail: qyx66@sdu.edu.cn; yinlw@sdu.edu.cn

DOI: 10.1002/adfm.201303080

seemed to be incorporating sulfur into mesoporous host (mostly carbon) structures to contain the polysulfides.[13,14] The obvious advantage of mesoporous structures is their small pore size and large overall pore volume. However, if the sulfur in the mesopores could still be accessed by electrolyte in which polysulfides may be dissolved, the active materials loss could only be alleviated, but not eliminated. This could be the reason that long-time stable capacity retention and high Coulombic efficiency for the related Li-S batteries were rarely reported. The second methodology was to use mesoporous silica as intermediate polysulfides absorber through weak bonding,[15] or using metal (such as copper and nickel) as sulfur absorber by forming metal-S alloys.[16] It was demonstrated that using a nickel current collector could improve the cyclability of sulfur cathode.[17] The true mechanism of such a good cyclability could be attributed to the formation of nickel sulfide, which could be speculated from the reported slope-shaped charge/discharge curves showing characteristic nickel sulfide behavior.[16]

Carbon aerogel (CA), as a novel and special type of porous carbon material with interconnected structure, and higher electrical conductivity.[17] The main characteristics of CA materials are their large surface area (400–900 m^2/g) and large pore volume (1–3 cm^3/g).[18,19] Due to its controllable three-dimensional porous structures, CA is believed to be an ideal electrode material for supercapacitors and rechargeable batteries due to their porous interconnected structure, high specific surface area. Importantly, the unique characteristic for CA materials is the abundant micropores and mesopores,[20,21] which can be utilized as a sulfur immobilizer host for sulfur impregnation for Li-S battery to effectively eliminate capacity fading effect due to the loss of sulfur cathode materials as a result of polysulfide dissolution.

In this work, the abundant pores, especially the micropores in the three-dimensional interconnected S/CA hybrids were utilized as immobilizer hosts for sulfur encapsulation. The highly electronically conductive CA matrices provide abundant micropores and high surface area to adsorb and disperse S and ameliorate its disadvantages, such as the insulating nature of S and the solubility of polysulfide intermediates in organic solvent based electrolytes. The elemental sulfur exists as a highly dispersed state inside the micropores of CA matrix. The obtained S/CA hybrid cathodes demonstrate superior cyclability and Coulombic efficiency, high rate cyclability. The S/CA hybrid with an optimal incorporating content of 27 wt% S shows an excellent performance of 820 $mAhg^{-1}$ after 50 cycles at the current density of 100 mAg^{-1}, even at the current density of 4C (6700 mAg^{-1}), the capacity still maintains at a value of 521 $mAhg^{-1}$ after 50 cycles. The long time stable cyclability, high capacities obtained at high rates of 3.2 C are attributed to the unique S/CA electrode architecture facilitating charge transport, and the trapping of polysulfides and cycled products within the pores in the CA electrode materials.

2. Results and Discussion

2.1. XRD Characterization of the S/CA Hybrid Samples

Figure 1 shows the typical X-ray diffraction (XRD) patterns of standard crystalline sulfur, as-prepared CA and S/CA hybrids.

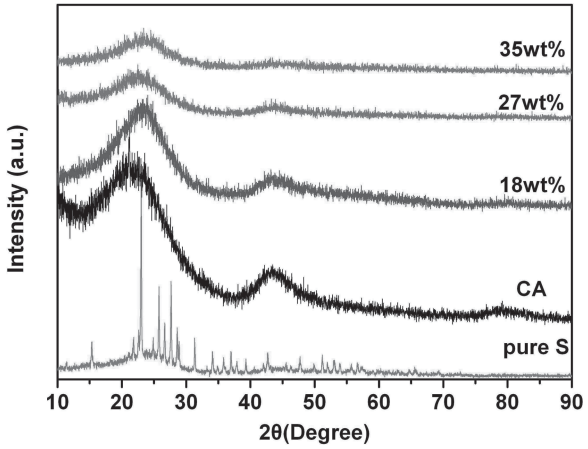

Figure 1. XRD patterns for CA, pure S and S/CA hybrids with 18, 27, 35% incorporated contents of S.

The presence of the broad (002) and (100) peaks in XRD pattern of CA sample suggests an amorphous state. It is indicated that there does not exist any apparent crystalline peak associated with sulfur in the XRD pattern of the S/CA hybrids, only two (002) and (100) peaks corresponding to amorphous structured carbon appear. An interesting phenomenon is that the intensity related to (002) and (100) peaks of becomes weaker with the content of S in the S/CA hybrids increasing. The microstructure characteristic, chemical composition and chemical bonding state of the S/CA hybrids can be further investigated and discussed in the following section.

2.2. The Nitrogen Adsorption–Desorption Isotherm Characterization of the S/CA Hybrid Samples

Figure 2 depicts the nitrogen adsorption–desorption isotherms, showing the Brunauer–Emmett–Teller (BET) specific surface area and porous characteristics of the S/CA hybrids. From Figure 2a, it is shown that the three curves of the *x*% S/CA hybrids (*x* = 18%, 27%, 35%), show a similar shape like pure CA sample. They exhibit a typical type IV isotherm with a H_1 hysteresis loop, indicating a disordered mesoporous structure for the S/CA samples. Figure 2b depicts the pore size distribution of the S/CA hybrids. The main peak of the size distribution changes gradually with the incorporation content of S in S/CA hybrids increasing. Compared with pure CA sample, the peak at 2 nm associated with the micropores almost disappears after encapsulating S into CA matrix, suggesting that the micropores of CA matrix are all occupied by the incorporated S nanoparticles.

The textual parameters including the BET specific surface area, pore diameter, total pore volume and micropore volume of the mesoporous CA and S/CA hybrids are summarized in **Table 1**. With the incorporation of S into the 3D CA framwork, S nanoparticles with several nanometers may first occupy the sites of micropores, whose volume is about 18% of the whole porous volume of the CA matrix, this directly leads to a rapid decrease of the number of the micropores. With more and more S incorporated, almost all the micropores are occupied and the microporous volume decrease to almost zero as

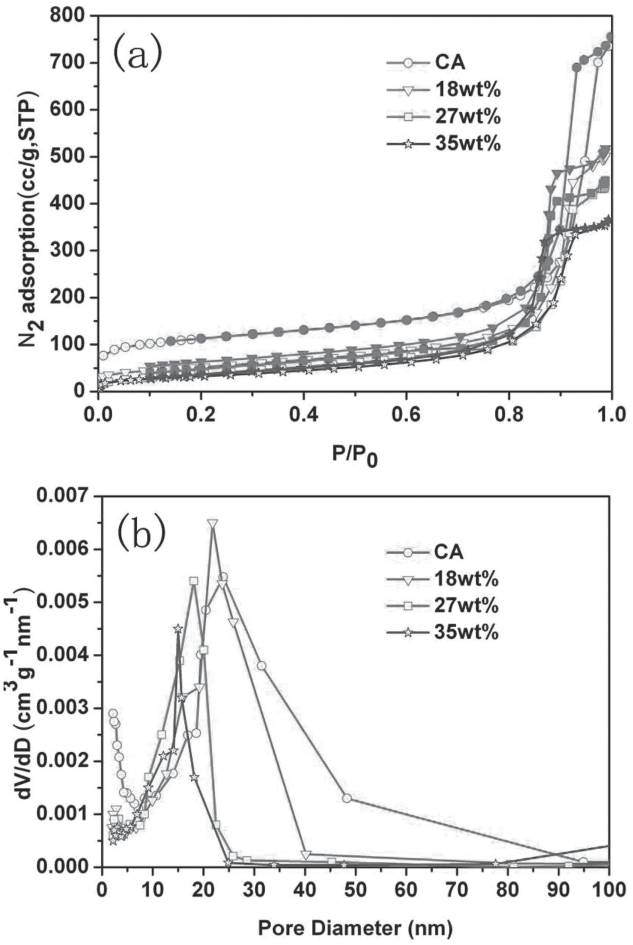

Figure 2. (a) N_2 adsorption-desorption isotherms samples of CA and S/CA hybrid (closed symbols: adsorption; open symbols: desorption). (b) Pore size distributions.

the content of S is 35%. After the microporous positions are occupied, S nanoparticles can easily enter into the position of mesopores, some of S nanoparticles may also easily distribute at the surfaces of CA matrix, this causes the decrease of surface area, porous volume, average poroes size.

With the S content increasing, the surface area of S/CA hybrids decreases from 642 for pure CA to 217, 203, and 187 m^2g^{-1} for incorporated 18%, 27%, and 35%S/CA hybrids. The pore diameter of S/CA hybrids displays a similar trend as that of surface area, decreasing from 16.5 for CA to 15.8, 14.1 and 12.6 nm for incorporated 18%, 27%, and 35% S/CA hybrids. The micropore volume of CA is 0.214 cm^3g^{-1}, the 18%S/CA hybrid decreases to only 0.014 for 18%S/CA hybrid. For the 35%S/CA hybrid, the micoropore volume is zero. It is believed that the reduction of micropore volume is advantageous to reduce irreversible capacity of lithium battery. The decrease of the surface area, pore diameter, total pore volume and micropore volume of the S/CA hybrids with the S content increasing, is due to incorporated S nanoparticles occupy almost all the micropores and some of the mesoporous pores.

2.3. XPS Characterization of the S/CA Hybrids

In order to further describe the chemical composition component and chemical bonding state of the S/CA hybrids, X-ray photoelectron spectroscopy (XPS) characterization on the S/CA hybrids was carried out. The overall XPS spectrum for the synthesized the 27 wt% S/CA hybrid sample in **Figure 3**a shows that the product is consisted of S, O, and C elements. The XPS elemental analysis suggests that the atom content of elemental sulfur is 12.1%, which agrees well with the calculated value 27 wt% of S content. The S content of other two S/CA hybrids can be determined via XPS analysis to be 18 wt% and 35 wt%, respectively. Figure 3b depicts the XPS spectrum of C 1s, a symmetrical peak at 284.3 eV corresponds well to amorphous carbon structure.[22] Figure 3c and 3d show the experimental and matched S 2p spectrum. Two peaks located in Figure 3d at 163.6 eV and 164.7 eV correspond to that of S and S_8, matching well with the S 2p spectrum. The XPS analysis result confirms that sulfur exist as a highly dispersed state with a low-molecular monolayered in the hybrid. The present XPS result is in agreement with the results by Demir and Guo et al. that the S 2p3/2 (163.6 and 164.8 eV) spin orbit level with an energy separation of 1.2 eV in the S 2p spectrum, is attributed to the S-S bond species.[23–27]

2.4. Raman Spectra of the S/CA Hybrids

The Raman spectra of pure CA and S/CA hybrid samples are given in **Figure 4**. Two peaks are observed at 1323 and 1588 cm^{-1} for pure CA sample, respectively. The peak at 1323 cm^{-1} (D band) is attributed to the Raman active *E*2g mode of the graphitic carbon lattice vibration, and the peak at 1350 cm^{-1} (G band) corresponds to the *A*1g mode of disordered carbon, which is considered to originate from some kind of imperfection.[28] For the graphitization degree of the carbon materials, it is generally evaluated according to the ratio of the intensity of the D band (I_D) to G (I_g) band (I_D/I_G). The I_D is higher than I_G in the spectrum of pure CA sample, indicating that CA sample has a structure with a fraction of graphitic cluster dispersed in disordered carbon.[29]

Table 1. Textural parameters of the CA and S/CA hybrid.

Sample	BET surface area [m^2g^{-1}]	Pore diameter [nm]	Total pore volume [cm^3g^{-1}]	Micropore volume [cm^3g^{-1}]
CA	642	16.5	1.02	0.214
18 wt%	217	15.8	0.851	0.014
27 wt%	203	14.1	0.752	0.005
35 wt%	187	12.6	0.600	0.001

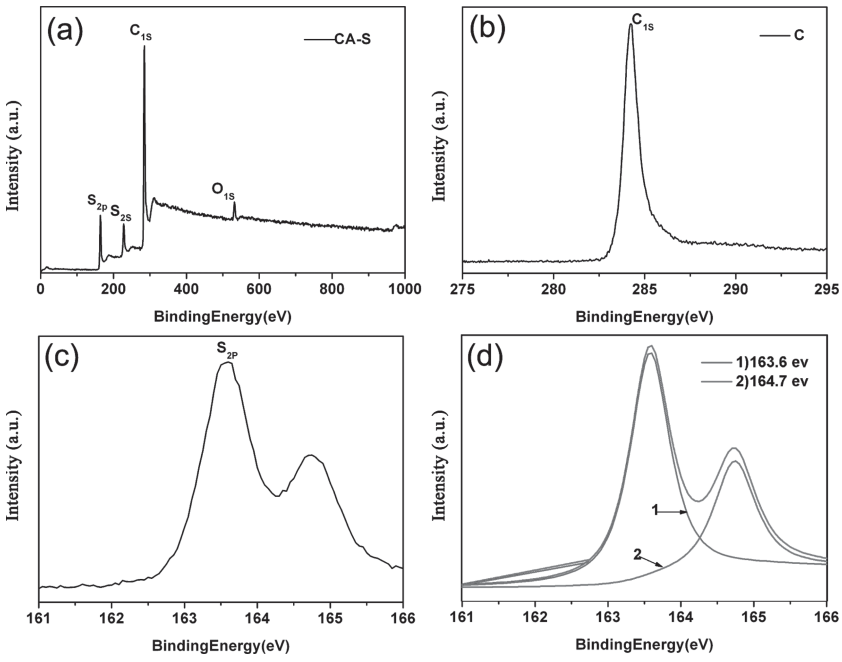

Figure 3. (a) Overall XPS spectrum of 27%S/CA hybrid. (b) XPS spectrum of C 1s. (c,d) Experimental and matched XPS spectrum of S 2p.

After encapsulation of S into three-dimensional interconnected CA matrix, a microstructure evolution takes place for the S/CA hybrids. The D band shifts from the 1323 to 1365 cm^{-1}, while the G band shifts from 1588 to 1603 cm^{-1}. Furthermore, the intensity of I_D decreases and the intensity of I_G increases relatively, so the ratio for the I_D to I_G (I_D/I_G) decreases compared with that of pure CA sample. The ratio of I_D/I_G is sensitive to the ratio of the concentration of graphite edge planes and/or crystal boundaries to standard graphite planes. The value of I_D/I_G is found to be 1.11, 0.93, and 0.91 for CA, 18%S/CA, 35%S/CA hybrid samples, respectively. This shows that the S/CA hybrids are more disordered after the incorporation of sulfur into the pores of CA matrix.[30]

2.5. EIS Spectra of the S/CA Hybrid Samples

The electrochemical impedance spectrum (EIS) was used to investigate the charge transport kinetics for the electrochemical properties of the S/CA hybrid samples. **Figure 5** shows the Nyquist profiles of the AC impedance for CA and 27%S/CA hybrid samples. Both the curves exhibit a semicircle in the high frequency region which is attributed to the ohmic resistance, and charge transfer resistance and a straight line in low frequency region which is related to the diffusion of lithium ions in the anode materials. The diameter of the semicircle on Z_{re} axis provides an approximate indication of the charge transfer resistance (Rct). The diameter of the semicircle of 27%S/CA hybrid is much smaller than that of pure CA smaple, indicating that the mesoporous three-diemnsional CA material can facilitate electron transfer from embedded S nanoparticles within the whole electrode and thus decrease resistance. The decrease of charge transfer resistance is profitable to improve the electron and ion kinetics in the composite electrode, consequently, enhancing the electrochemical performance of the S/CA hybrids.

2.6. SEM and TEM Characterization of the S/CA Hybrid Samples

The microstructures of the CA materials are observed by field emission scanning electron microscopy (FE-SEM) and transmission electron microscopy (TEM), as shown in Figure S1. The CA materials are composed of carbon spheres interconnecting each other, forming a 3D network architectural structure. It is shown that the average size of the CA nanoparticles is 20 nm (TEM image for CA in Figure S1), the CA sample displays

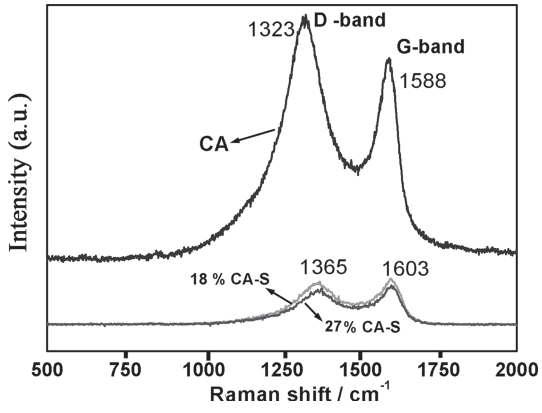

Figure 4. Raman spectra from the CA, S/CA hybrids with incorporated 18% and 35% S.

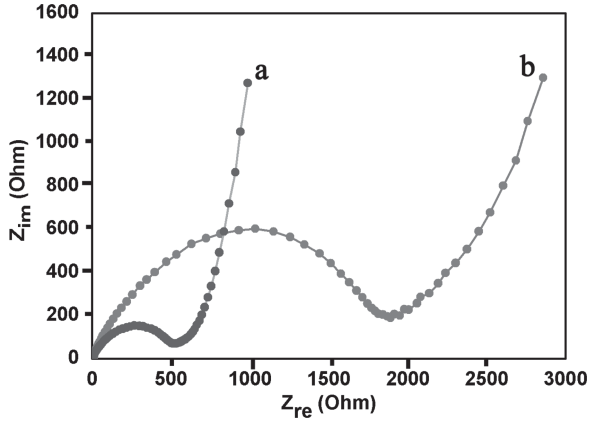

Figure 5. EIS spectra of (a) 27%S/CA hybrid and (b) S sample.

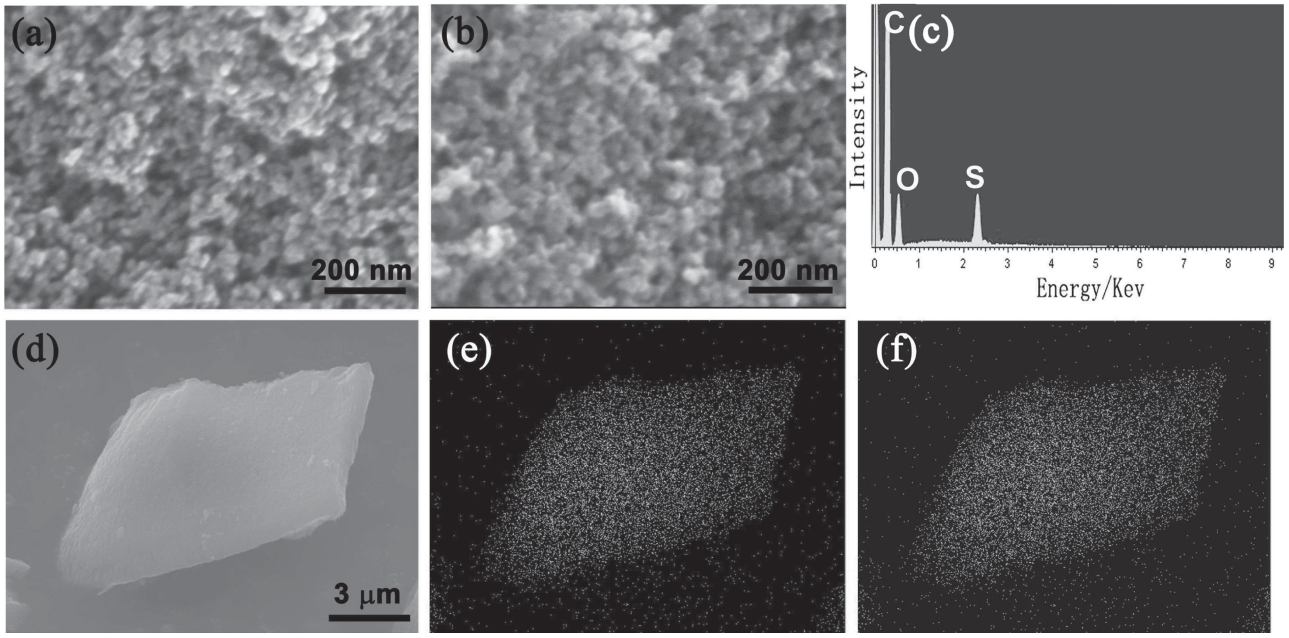

Figure 6. FE-SEM images of (a) CA and (b) 27%S/CA hybrid. (c) A typical EDS spectrum for the synthesized S/CA. (d) Low magnification SEM image, (e,f) S and C elemental mapping.

interconnected structures with abundant of mesopores and micropores.

Figure 6a,b show the field emission scanning electron microscopy (FE-SEM) images of CA and 27%S/CA hybrid samples. It is obviously indicated that the S/CA hybrid still keeps three-dimensional porous structure after encapsulating sulfur. A typical EDS spectrum from the 27%S/CA hybrid suggests that the hybrid is composed of C, S, and small amount of O elements. Figure 5e,f demonstrates the S- and C elemental mapping of the S/CA hybrid, showing that C and S are homogeneously distributed among the whole hybrid samples.

Figure 7a shows a low TEM image of the 18%S/CA hybrid. It is indicated the hybrid can still maintains a typical interconnected product with a homogeneous distribution for S and CA components. The high magnification TEM image in Figure 7b demonstrates the detail microstructures of the 18%S/CA hybrid sample. Two kinds of nanoparticles with different color contrasts are connected each other, the smaller S nanoparticles with dark color are embedded in the connected CA matrices with grey color. The TEM image in Figure 7c is the magnified microstructure of the S/CA hybrid. The S nanoparticles about 5–10 nm with dark color are embedded in interconnected CA framework matrices with grey color. Compared with the pure CA sample, it is shown that the due to the incorporation of S nanoparticles in CA matrices, some of the micropores and a part of the mesopores of the CA matrices (Figure 7b,c) are occupied. A high resolution TEM (HRTEM) lattice image in Figure 7d of the microstructures of the S/CA hybrid shows an arrangement of mostly disordered sp^2 carbon fringes for CA. The mesopores with an average size of 8–13 nm revealed in magnified TEM images (Figure 7d and **Figure 8**d) is in good agreement with the nitrogen physisorption analysis. The amorphous S is distributed in CA matrices.

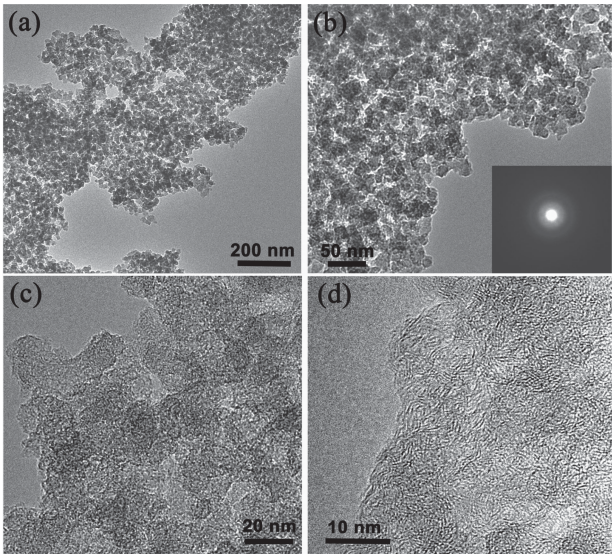

Figure 7. (a,b) Low- and (c) high-magnification TEM images, the down right side inset in (b) is electron diffraction pattern. (d) High-resolution TEM lattice image of 18%S/CA hybrid.

Figure 8 depicts the TEM microstructures of 27%S/CA hybrid. The low magnification TEM images of 27%S/CA hybrid in Figure 8a,b shows that S nanoparticles with dark contrast are embedded in CA matrices. With the S content increasing, almost most of the micropores are depleted, more and more S nanoparticles are embedded within the mesopores of CA matrices, and the number and size of the mesopores decreases (Figure 8c,d). From the high magnification TEM images of 18%, and 27%S/CA hybrids in Figure 7d and 8d, it shows that

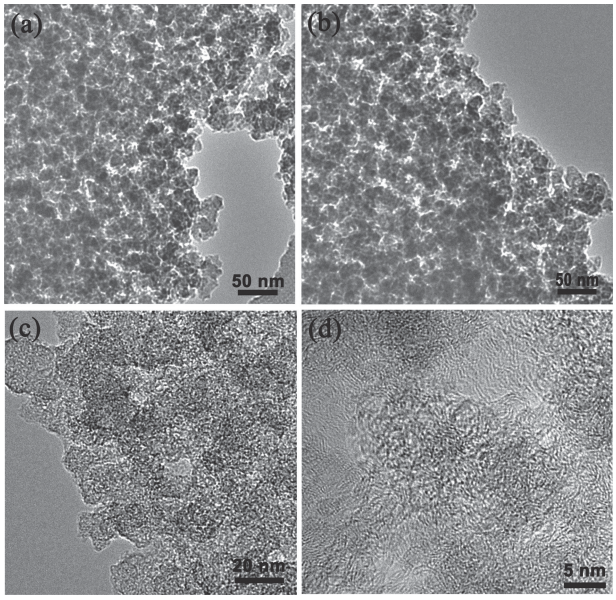

Figure 8. (a,b) Low- and (c) high-magnification TEM images. (d) High-resolution TEM lattice image of 27%S/CA hybrid.

the S components are embedded within the CA matrices. It is clearly revealed from Figure 8d that because some of the amorphous S phase components are entrapped within pore channels of the CA matrices, almost all the micropores are filled with S amorphous nanoparticles for the 27%S/CA hybrids compared with the 18%S/CA hybrid. The microstructures revealed in Figure 7 and Figure 8 are in good agreement with the nitrogen adsorption-desorption isotherm characterization.

2.7. Electrochemical Characterization of the S/CA Hybrid Samples

Figure 9 shows the cyclic voltammetric (CV) curves of the first three cycles of the S/CA hybrids at a scan rate of 0.1 mV s^{-1} between 1.0–3.0 V. It is reported that the redox reaction of elemental sulfur (S_8) is stepwise and complex,[31] a typical CV behavior of sulfur cathode can be divided into three steps: S_8 to S_6^{2-}, S_4^{2-}, and S_2^{2-} (or S^{2-}), respectively. From Figure 9a, the cathodic peak at 2.03 V (vs Li+/Li) in the first CV curve of 18%S/CA hybrid sample is associated with the elemental sulfur (S_8) to lithium ploysulfide anions (Li_2S_n, where n is typically 4–6).[32–34] Another cathodic peak at 1.22 V can be attributed to a further reduction of polysulfide ions to insoluble Li_2S_2/Li_2S. The two step reduction reactions may be described as: $S_8 + 4Li+ + 4e^- = 2Li_2S_4$, $Li_2S_4 + 4Li+ + 4e^- = 2Li_2S + Li_2S_2$.[35] An important phenomenon is that with the S content increasing, the reduction peak at 1.22 V of the 18%S/CA hybrids in the first scan shift to positions at higher potential of 1.36 V and 1.42 V for 27%, 35%S/CA hybrids, while the initial reduction peak at 2.03 V shifts to 1.92 and 1.93 V, respectively (Figure 9b,c). In the first anodic scan, an oxidation peak was observed at 2.41 V for the 18%S/CA hybrid (Figure 9a), which can be attributed to the conversion of Li_2S to lithium polysulfide. It is noted that for the

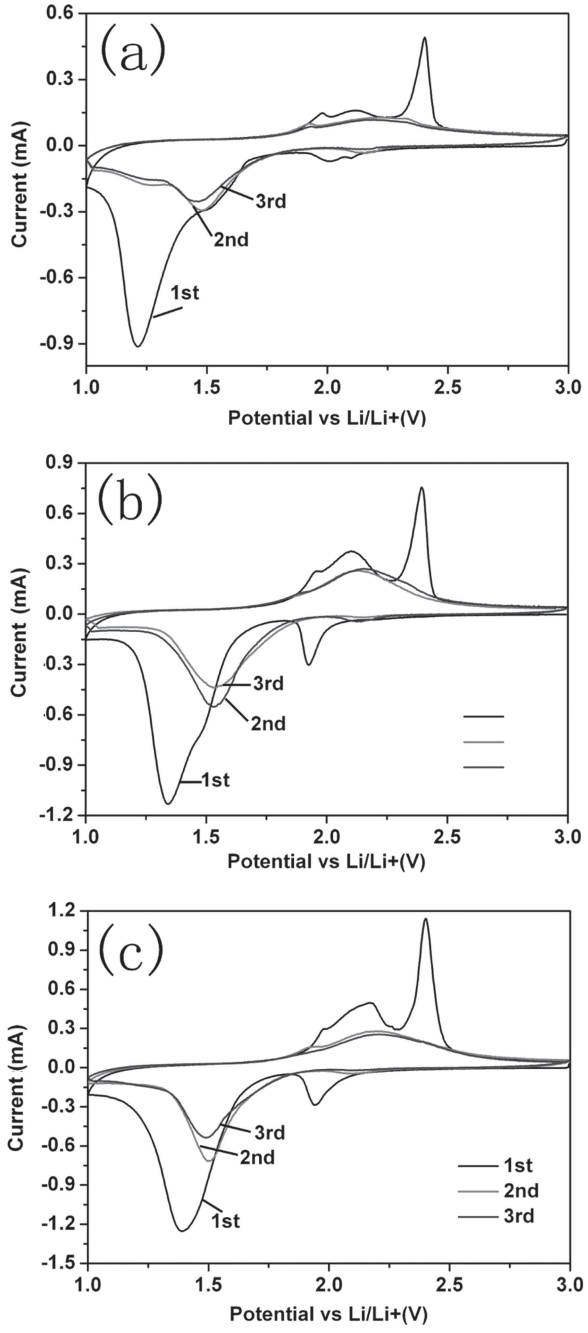

Figure 9. Cyclic voltammetric (CV) curves of the first three cycles for S/CA hybrids: (a) 18 wt%, (b) 27 wt%, (c) 35 wt%, at a scan rate of 0.1 mV s^{-1} between 1.0 and 3.0 V.

anodic peak of the S/CA hybrids, with the S content increasing, the intensity of initial anode peak at 2.41 V becomes stronger, as shown in Figure 9b,9c.

In the second CV scan, it is shown that the cathodic peak at around 2.0 V disappears for all the S/CA samples, while the cathodic peak at 1.22 V of the initial cathodic peak shifts to the position at about 1.5 V, and the current of the corresponding peak decreases to a low value. In the subsequent second anodic cycle, the oxidation peak shifts to the position at 2.21 V, while

the intensity of the anode peak gets weaker and broader, which is believed to be attributed to the complete conversion of Li_2S and polysulfides into elemental S. While Jayaprakash et al. believed that the oxidation peak at 2.21 V is associated with the formation of Li_2Sn ($n > 2$).[32,33]

With the increase in cycle number, it is shown that the main reduction peak shifts to slightly higher potential and the oxidation peak shifts to lower potentials, indicating an improvement of reversibility of the cell with cycling. After the 2nd cycles, the voltage and peak current density of the cathodic and anodic peaks for the S/CA hybrid keeps almost constant, showing the stable electrochemical performance of the hybrids.[12] The irreversibility of the second peak corresponds to the formation of a solid electrolyte interphase (SEI) layer on the CA surface and decomposition of electrolyte solvent between the electrode and electrolyte.[36] From the second cycle, the anode peak shifts to the position at 2.21 V, while the intensity of the anode peak gets weaker and broader. It should be pointed that the reduction and oxidation peaks are not one-to-one and do not matches well with that as expected for a conventional battery system. The detailed mechanisms for oxidation and reduction of sulfur, polysulfides and lithium sulfide during charge/discharge were already reported.[37–39]

Figure 10a–c shows the initial five discharge/charge curves of *x*%S/CA ($x = 18, 27, 35\%$) hybrid electrodes at the current density of 100 mAg^{-1} between 1.0V and 3.0V at room temperature. The hybrid electrodes show initial discharge capacity of 2264, 2061 and 1929 $mAhg^{-1}$ for 18%, 27%, and 35%S/CA hybrids, while the initial charge capacity of the corresponding hybrids is 1077, 1230, 1367 $mAhg^{-1}$, corresponding to the initial coulombic efficiency of 47.6%, 59.7%, 70.8%, respectively. The loss in capacity could be attributed to the formation of a solid eletrolyte interface (SEI) and the irreversible reaction of the samples. At the 5th cycle, the S/CA hybrids display discharge capacity of 870, 809, and 730 $mAhg^{-1}$ for 18%, 27% and 35%S/CA hybrids, while the charge capacity of the corresponding hybrids is only 805, 777, 713 $mAhg^{-1}$, corresponding to coulombic efficiency of 92.5%, 96.2%, 97.7%, respectively. It is shown that reversible capacity and coulombic efficiency increases with the S content increasing. However, in the subsequent cycling, with the increase of S content, the irreversible capacity of the S/CA hybrids first rapidly increases and then decreases as the S content is up to 27%.

According to the first five discharge/charge curves in Figure 10, all discharge/charge curves of the three S/CA hybrids show two plateaus at 1.9–2.1 V and 1.2–1.6 V in the first discharge curves corresponding to the initial cathodic peaks during cyclic voltammetric process described in Figure 9. Another plateau at about 2.4 V in the first charge curves is agreement with the anodic peak in the cyclic voltammetric process in Figure 9. It should be specially pointed that the high voltage plateaus almost disappear in the following cycles, which is also in agreement with the CV curves.

Figure 11 comparatively describes the cycling performance and stability of the S/CA hybrids with different S loading contents, at a galvanostatic charge/discharge current of 100 mA g^{-1} between 1.0 and 3.0 V. As described above, the hybrid electrodes show initial discharge capacity of 2264, 2368, and 1929 $mAhg^{-1}$ for 18%, 27% and 35% incorporated S/CA

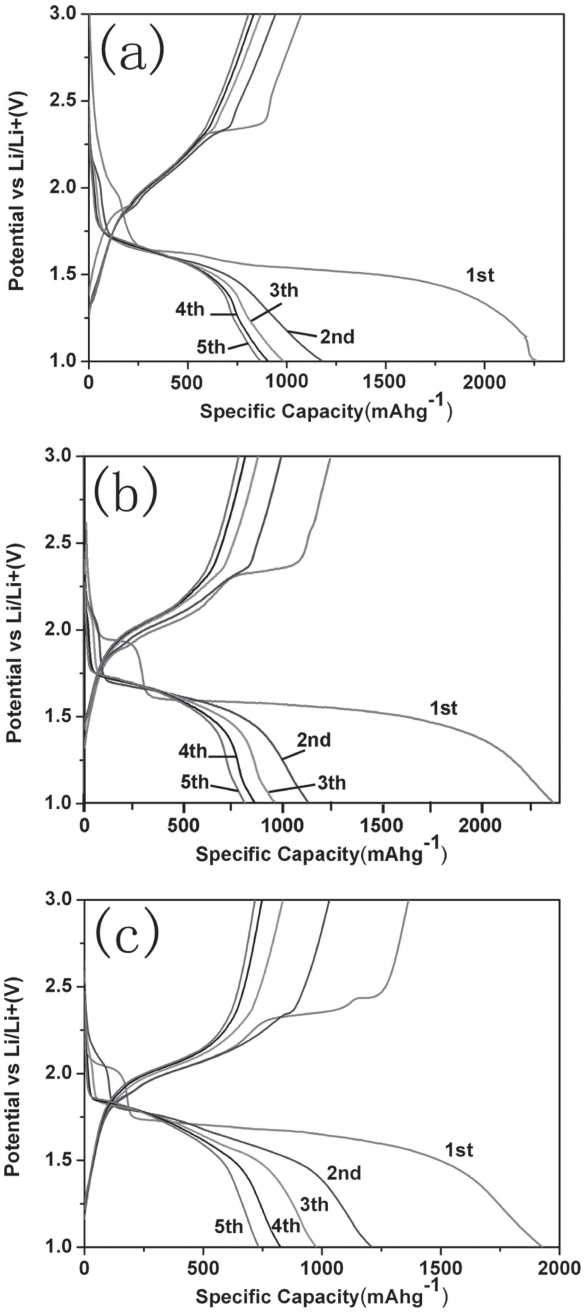

Figure 10. Electrochemical performances of S/CA hybrid: the initial five charge-discharge curves between 1.0 V and 3.0 V at the current of 100 mAg^{-1} for (a) 18 wt%. (b) 27 wt%. (c) 35 wt%.

hybrids, while the charge capacity of the corresponding hybrids is 1077, 1441, 1367 $mAhg^{-1}$, corresponding to the initial coulombic efficiency of 47.6%, 60.9%, 70.8%, respectively. The hybrid electrodes show the 10th discharge capacity of 811, 877, and 721 $mAhg^{-1}$ for 18%, 27% and 35% S/CA hybrids, while the 10th charge capacity of the corresponding hybrids is 800, 867, 712 $mAhg^{-1}$, corresponding to coulombic efficiencies of 98.6%, 98.9%, and 98.7%, respectively.

After 10 cycles, the specific capacity of S/CA hybrid samples tends to be stable. The 20th discharge and charge capacity of

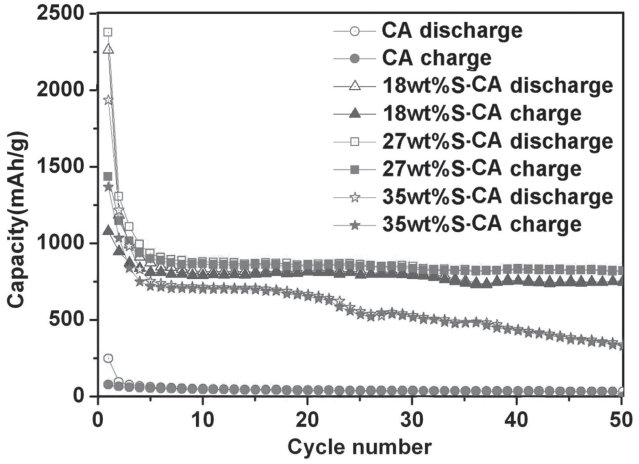

Figure 11. Capacity vs. cycle number curves of S/CA hybrid between 1.0 V and 3.0 V at the discharge current of 100 mAg^{-1}.

is 831 and 821, 865, and 857 $mAhg^{-1}$ for the 18%, 27% S/CA hybrids, respectively. While for the 35%S/CA hybrid, it shows a discharge and charge capacity of 651 and 641 $mAhg^{-1}$, corresponding to a coulombic efficiency of 98.5. At the 30 cycle, the 35%S/CA hybrid displays a reversible capacity of 520 $mAhg^{-1}$, while the reversible capacity is still 840 $mAhg^{-1}$ for 27%S/CA hybrid cathode. At the 50th cycle, the hybrids show a 50th discharge capacity of 755, 822, and 340 $mAhg^{-1}$ for 18%, 27% and 35% incorporated S/CA hybrids, and a charge capacity of 748, 820, 335 $mAhg^{-1}$ for the corresponding hybrids, with a coulombic efficiency of 99.1%, 99.9%, 98.5%, respectively. Compared with pure CA sample, the S/CA hybrid samples show greatly enhanced electrochemical performance. For pure CA sample, the first discharge and charge capacity are 252.9 and 78 mAh g^{-1}; the 5th discharge and charge capacity are only 67 and 61 mAh g^{-1}. At the 10th cycle, CA displays a stable capacity of 50 mAh g^{-1}. At 50th cycle, it only remains a specific capacity of 25 mAh g^{-1}. From the Figure 11, it is seen that the capacity of S/CA hybrid decrease quickly at the beginning, after about five cycles, the reversible capacity tends to be stable, the 27%S/CA hybrid cathode shows a excellent reversible capacity of 820 mAh g^{-1}, but as the S content increases to 35 wt%, the capacity can't remain stable due to the blocking of micropores and the excess of sulfur on the surface.

The presently reported electrochemical performance of the S/CA hybrids is superior to that of previously reported other S/carbon based nanocomposites. For example, Choi et al.[10] reported a discharge capacity of about 500 $mAhg^{-1}$ until 50th cycle for the carbon-coated sulfur cathodes, which is two times larger than that of no-coated sulfur cathode. While for the sulfur-coated multi-walled carbon nanotubes composite cathode, it shows a reversible capacity of 670 $mAhg^{-1}$ after 60 cycles.[11] It is shown that by Wang[13] that the sulfur–mesoporous carbon composites could maintain a reversible capacity of 500 $mAhg^{-1}$ after 40 cycles. Recently, Rao's group[40] reported that porous carbon–sulfur composite with 53.7% S maintains a stable discharge capacity of more than 740 mA h g^{-1} after 100 cycles.

Figure 12 shows the rate capability of the S/CA hybrids. After 10 cycles at a current density of 0.1C (1C is 1675 $mAhg^{-1}$), the S/CA hybrid samples show the reversible capacity of 813, 958, and 711 mAh g^{-1} for 18%, 27%, and 35%S/CA hybrid samples. At a current density of 0.4 C, the 20th reversible capacity is 727, 822, and 679 $mAhg^{-1}$ for 18%, 27%, and 35% S/CA hybrid samples, respectively. Even after 50 cycles at a current density of 3.2 C, the reversible capacity of the hybrids are 444, 521, and 220 $mAhg^{-1}$ for 18%, 27%, and 35%S/CA hybrid samples. As the current density returns to 0.2C, the reversible specific capacity can remain at values of 814, 891 mAhg-1 for 18% and 27%S/CA hybrid samples, respectively. While for the 35%S/CA hybrid sample, as the current density returns to 0.2C, the 60th reversible capacity is 584 mAhg-1. As is seen, the S/CA hybrid with a incorporating S content of 27% presents good rate capability, at the high current density of 3.2 C, the S/CA hybrid keeps a stable reversible capacity of 521 mAhg-1, which is 2.37 times higher than that of 35%S/CA hybrid sample.

The improved electrochemical performance of the three-dimensional interconnected porous S/CA hierarchical hybrids can be attributed to their unique interconnected porous microstructures. **Figure 13** depicts the scheme of the discharge reaction model of the S/CA hybrid cathodes. The three dimensionally networked CA matrices in the S/CA hybrid samples serves as a useful electronic framework for elemental sulfur homogenous dispersion. EIS characterization suggests that the charge transfer ability during the charge/discharge process is much improved by the percolating electronic path of the CA network. The CA matrices with a good electrical conductivity can serve as the conductive channels between elemental sulfur, which decreases the inner resistance of battery and is favorable for stabilizing the electronic and ionic conductivity, therefore leading to a higher specific capacity.[41] The CA matrices contain abundant micropores which are disadvantageous to Li^+ transmission, but it is the paragon storage space for elemental sulfur, such the elemental sulfur could be highly dispersed inside the narrow micropores of CA matrices, which is beneficial to the excellent high rate discharge capability of the sulfur

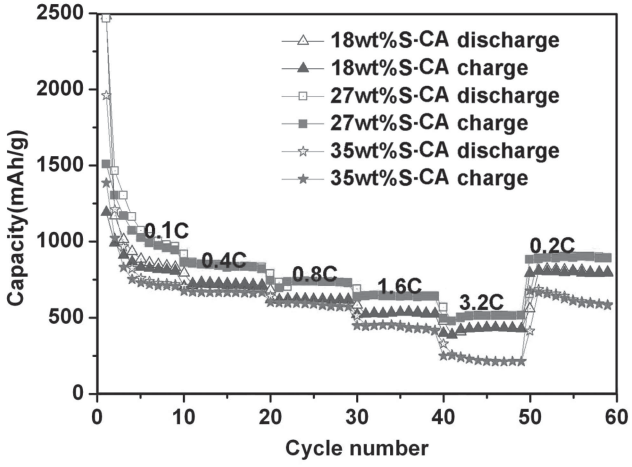

Figure 12. Rate capacity curves of S/CA hybrids between 1.0 V and 3.0 V at different current densities.

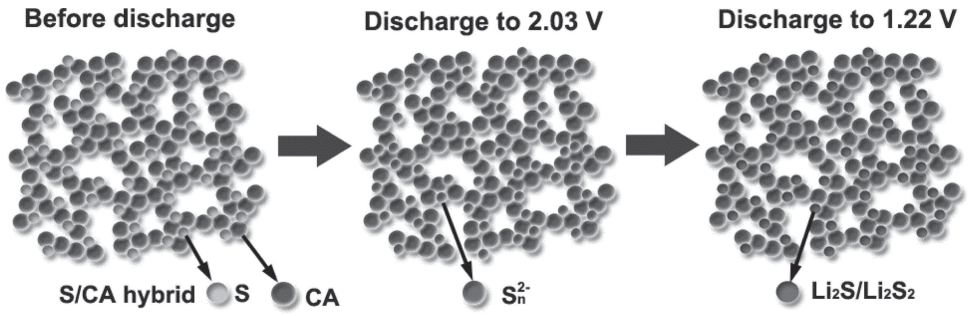

Figure 13. Scheme of the discharge reaction model of S/CA hybrid cathodes.

cathode owing to the good electrical conductivity of CA materials. Importantly, the narrow micropores of CA can trap stably elemental sulfur and subsequent lithium polysulfides during cycling due to such a strong adsorption, avoiding the shuttle reaction, mass loss of the active materials and the formation of the thicker Li2S insulating layer on the hybrid surface. Therefore, the electrochemical reaction constrained only inside the narrow micropores proposed here would be the dominant factor for the enhancement of the long electrochemical stability of the S/CA hybrid cathode.

3. Conclusions

We synthesized S/CA hybrid with high dispersed elemental S inside the micropores of CA matrix through a facile route. These porous S/CA hybrids were used as cathode electrodes for rechargeable Li-S batteries to evaluate their electrochemical performance. The highly electronically conductive CA matrices provide abundant micropores and high surface area to adsorb and disperse S and ameliorate its disadvantages, such as the insulating nature of S and the solubility of polysulfide intermediates in organic solvent based electrolytes. The S/CA hybrid with 27 wt% sulfur show excellent capacity retention f 820 $mAhg^{-1}$ after 50 cycles at a current density of 100 mAg^{-1}. Even at the current density of 3.2C (5280 mAg^{-1}), the reversible capacity of 27 wt%S/CA hybrid can still maintain at a reversible capacity of 521 $mAhg^{-1}$ after 50 cycles. It should be noted that the improved electrochemical performance owing to the three-dimensional microporous network and excellent electrical conductivity of CA matrix, the microporous network offer abundant space for elemental sulfur, such the sulfur exists as a highly dispersed state with a low-molecular monolayered coverage inside the micropores of CA, not only was the poor electric conductivity improved, but also the runoff of polysulphide was reduced.

4. Experimental Section

Preparation of the S/CA Hybrids: The carbon matrix (CA) were prepared according to the method reported by Shenet al.[42] In a typical synthesis, 5.5 g resorcinol (R) and 8.1 g formaldehyde (F) (37 wt%) were added to 14.75 g H_2O (the RF content was about 30 wt%), the mixture was stirred for 10 min. Then a certain amount of sodium carbonate (catalyst/C) was added to the above solution with a R/C ratio of 500. After 20 min continuously stirring, the mixture was transferred to a flat-bottom flask, sealed. For further gelation and aging, the samples were heat treated in a (1, 1, 1)-cycle, where the numbers stand for the days at room temperature, 50 °C and 90 °C, respectively. The RF gels were dried at ambient condition. The pyrolysis technique was used to transform the gels into carbon aerogels at 1000 °C with a heating rate of 3 °C min^{-1} and kept for 2 h under a nitrogen protecting gas flow. Sulfur-carbon aerogel (S/CA) hybrid materials were prepared by thermal treatment of a mixture of CA and elemental sulfur at 149 °C for 6 h in a sealed tube furnace filled in an argon gas flow. At the temperature, the molten sulfur with the lowest viscosity (0.00709 Pa s) can easily diffuse into the micropores of CA matrix. Then, the temperature was increased to and kept at 300 °C for 1, 2, 3 h to vaporize the superfluous sulfur on the outer surface of carbon spheres. After cooling down to room temperature, the S/CA hybrids were obtained, the sulfur content were controlled to be 18, 27, 35 wt%, respectively.

Sample Characterization: The x-ray diffraction (XRD) patterns of the products were determined by Rigaku D/Max-KA diffractometer equipped with Cu *Kα* radiation. The morphology and chemical components of the products were analyzed using SU-70 field emission scanning electron microscopy (FE-SEM). The morphology and microstructure of the synthesized products were analyzed using high-resolution transmission electron microscopy (HR-TEM) of JEM-2100 at an acceleration voltage of 200 kV. X-ray photoelectron spectroscopy (XPS) characterization was carried out in an ESCALAB 250 instrument with 150W Al Ka probe beam. Survey and multiregion spectra were recorded at S2p, C1s and O1s photoelectron peaks. Nitrogen adsorption-desorption isotherms were determined at 77 K using micromeritics ASAP 2020 surface area and porosity analyzer. The surface area measurements were performed according to the Brunauer-Emmett-Teller (BET) method. The pore size distribution was obtained from the desorption branch of isotherm using the corrected form of Kelvin equation by means of the Barrett-Joyner-Halenda (BJH) method. Raman spectra were measured and collected using a 632.8 nm laser with a JY HR800 under ambient conditions, with a laser spot size of about 1 μm.

Electrochemical Measurements: Working electrodes were prepared by mixing 80 wt% active material, 10 wt% acetylene black (Super-P), and 10 wt% polyvinylidene fluoride binder dissolved in N-methyl-2-pyrrolidinone. The galvanostatic charging/discharging tests were conducted using standard 2032 type coin cells with copper foil as the current collectors, lithium foil as reference electrodes and 1.0 M $LiPF_6$ in mixed ethylene carbonate (EC) and diethyl carbonate (DEC) (EC:DEC, 1:1 by volume) as the electrolyte. A cut-off voltage window of 1.0 – 3.0 V was used. The 2032 coin-type cells were assembled in an argon-filled glovebox with less than 1 ppm of oxygen and water, galvanostatically cycled on a LAND CT2001A instrument (Wuhan, China) at room temperature. Cyclic voltammetry (CV) study was conducted using an electrochemical workstation (PARSTAT 2273) between 1.0–3.0 V at a scan rate of 0.1 mV s^{-1}.

Supporting Information

Supporting Information is available from the Wiley Online Library or from the author.

Acknowledgements

We acknowledge support from the National Natural Science Funds for Distinguished Young Scholars (No: 51025211), The National Basic Research Program (No: 2013CB934303), National Nature Science Foundation of China (No: 51272137), the Tai Shan Scholar Foundation of Shandong Province.

Received: September 3, 2013
Revised: October 23, 2013
Published online: December 23, 2013

[1] V. Etacheri, R. Marom, R. Elazari, G. Salitra, D. Aurbach, *Energ. Environ. Sci.* **2011**, *4*, 3243–3262.
[2] B. Scrosati, J. Hassoun, Y. K. Sun, *Energ. Environ. Sci.* **2011**, *4*, 3287–3295.
[3] J. B. Goodenough, Y. Kim, *Chem. Mater.* **2009**, *22*, 587–603.
[4] J. M. Tarascon, M. Armand, *Nature* **2001**, *414*, 359–367.
[5] R. D. Rauh, K. M. Abraham, G. F. Pearson, J. K. Surprenant, S. B. Brummer, *J. Electrochem. Soc.* **1979**, *126*, 523–527.
[6] K. Kang, Y. S. Meng, J. Bréger, C. P. Grey, G. Ceder, *Science* **2006**, *311*, 977–980.
[7] L. Yuan, X. Qiu, L. Chen, W. Zhu, *J. Power Sources* **2009**, *189*, 127–132.
[8] B. Scrosati, J. Garche, *J. Power Sources* **2010**, *195*, 2419–2430.
[9] X. Ji, L. F. Nazar, *J. Mater. Chem.* **2010**, *20*, 9821–9826.
[10] Y. J. Choi, Y. D. Chung, C. Y. Baek, K. W. Kim, H. J. Ahn, *J. Power Sources* **2008**, *184*, 548–552.
[11] L. Yuan, H. Yuan, X. Qiu, L. Chen, W. Zhu, *J. Power Sources* **2009**, *189*, 1141–1146.
[12] D. Marmorstein, T. H. Yu, K. A. Striebel, F. R. McLarnon, J. Hou, E. J. Cairns, *J. Power Sources* **2000**, *89*, 219–226.
[13] J. Wang, S. Y. Chew, Z. W. Zhao, S. Ashraf, D. Wexler, J. Chen, S. H. Ng, S. L. Chou, H. K. Liu, *Carbon* **2008**, *46*, 229–235.
[14] X. Ji, K. T. Lee, L. F. Nazar, *Nat. Mater.* **2009**, *8*, 500–506.
[15] X. Ji, S. Evers, R. Black, L. F. Nazar, *Nat. Commun.* **2011**, *2*, 325.
[16] S.-C. Han, H.-S. Kim, M.-S. Song, P. S. Lee, J.-Y. Lee, H. J. Ahn, *J. Alloy. Compound.* **2003**, *349*, 290–296.
[17] a) F. B. Hao, Z. W. Zhang, L. W. Yin *ACS Appl. Mater. Interfaces* **2013**, *5*, 8337–8344; b) X. Lu, O. Nilsson, J. Fricke, R. W. Pekala, *J. Appl. Phys.* **1993**, *73*, 581–584.
[18] Y. Hanzawa, K. Kaneko, R. W. Pekala, M. S. Dresselhaus, *Langmuir* **1996**, *12*, 6167–6175.
[19] D. Wu, Z. Sun, R. Fu, *J. Appl. Polymer Sci.* **2006**, *99*, 2263–2267.
[20] J. Shen, J. Hou, Y. Guo, H. Xue, G. Wu, B. Zhou, *J. Sol-Gel Sci. Tech.* **2005**, *36*, 131–136.
[21] J. Wang, S. Q. Zhang, J. Shen, Y. Z. Guo, S. M. Attia, B. Zhou, Z. Q. Lai, G. Z. Zheng, Y. S. Gui, *J. Porous Mater.* **2001**, *8*, 167–170.
[22] H. Ago, T. Kugler, F. Cacialli, W. R. Salaneck, M. S. P. Shaffer, A. H. Windle, R. H. Friend, *J. Phys. Chem. B* **1999**, *103*, 8116–8121.
[23] R. Demir-Cakan, M. Morcrette, F. Nouar, C. Davoisne, T. Devic, D. Gonbeau, R. Dominko, C. Serre, G. Ferey, J. M. Tarascon, *J. Am. Chem. Soc.* **2011**, *133*, 16154–16160.
[24] L. Zhang, L. Ji, P. A. Glans, Y. Zhang, J. Zhu, J. Guo, *Phys. Chem. Chem. Phys.* **2012**, *14*, 13670–13675.
[25] B. K. Guo, B. Teng, Z. H. Bi, G. M. Veith, X. G. Sun, S. L. Qiu, S. Dai, *Chem. Commun.* **2013**, *49*, 4905–4907.
[26] A. G. Schaufuß, H. W. Nesbitt, I. Kartio, K. Laajalehto, G. M. Bancroft, R. Szargan, *J. Electron Spectrosc. Relat. Phenom.* **1998**, *96*, 69–82.
[27] G. M. Zhou, L. C. Yin, D. W. Wang, L. Li, S. S. F Pei, I. R. Gentle, F. Li, H. M. Cheng, *ACS Nano* **2013**, *6*, 5367–5375.
[28] S. Evers, L. F. Nazar, *Chem. Commun.* **2012**, *48*, 1233–1235.
[29] J. C. Guo, Y. H. Xu, C. S. Wang, *Nano Lett.* **2011**, *11*, 4288–4294.
[30] T. Bordjiba, M. Mohamedi, Lê. H. Dao, *Adv. Mater.* **2008**, *20*, 815–819.
[31] H. Yamin, A. Gorenshtein, J. Penciner, Y. Sternberg, E. Peled, *J. Electrochem. Soc.* **1988**, *135*, 1045–1048.
[32] N. Jayaprakash, J. Shen, S. S. Moganty, A. Corona, L. A. Archer, *Angew. Chem. Int. Ed.* **2011**, *50*, 5904–5908.
[33] B. Zhang, C. Lai, Z. Zhou, X. P. Gao, *Electrochimica Acta* **2009**, *54*, 3708–3713.
[34] Y. Cao, X. Li, I. A. Aksay, J. Lemmon, Z. Nie, Z. Yang, J. Liu, *Phys. Chem. Chem. Phys.* **2011**, *13*, 7660–7665.
[35] a) R. Elazari, G. Salitra, A. Garsuch, A. Panchenko, D. Aurbach, *Adv. Mater.* **2011**, *23*, 5641–5644; b) J. C. Guo, Y. H. Xu, C. S. Wang, *Nano Lett.* **2011**, *11*, 4288–4294.
[36] W. Yao, J. Yang, J. Wang, L. Tao, *Electrochimica Acta* **2008**, *53*, 7326–7330.
[37] J. Shim, K. A. Striebel, E. J. Cairns, *J. Electrochem. Soc.* **2002**, *149*, A1321–A1325.
[38] D. Li, F. Han, S. Wang, F. Cheng, Q. Sun, W. C. Li, *ACS Appl. Mater. Interfaces* **2013**, 2208–2213.
[39] L. W. Ji, M. M. Rao, H. M. Zheng, L. Zhang, Y. C. Li, W. H. Duan, J. H. Guo, E. J. Cairns, Y. G. Zhang, *J. Am. Chem. Soc.* **2011**, *133*, 18522–18525
[40] M. M. Rao, W. S. Li, E. J. Cairns, *Electrochem. Comm.* **2012**, *17*, 1–5.
[41] W. Zhou, C. Cheng, J. Liu, Y. Y. Tay, J. Jiang, X. Jia, J. Zhang, H. Gong, H. H. Hng, T. Yu, H. J. Fan, *Adv. Funct. Mater.* **2011**, *21*, 2439–2445.
[42] J. Shen, J. Wang, J. Zhai, Y. Guo, G. Wu, B. Zhou, X. Ni, *J. Sol-Gel Sci. Tech.* **2004**, *31*, 209–213.